

Ge Bidirectional Diffusion to Simultaneously Engineer Back Interface and Bulk Defects in the Absorber for Efficient CZTSSe Solar Cells

Jinlin Wang, Jiazheng Zhou, Xiao Xu, Fanqi Meng, Chunxu Xiang, Licheng Lou, Kang Yin, Biwen Duan, Huijue Wu, Jiangjian Shi, Yanhong Luo, Dongmei Li,* Hao Xin,* and Qingbo Meng*

Aiming at a large open-circuit voltage (V_{OC}) deficit in $Cu_2ZnSn(S,Se)_4$ (CZTSSe) solar cells, a new and effective strategy to simultaneously regulate the back interface and restrain bulk defects of CZTSSe absorbers is developed by directly introducing a thin GeO_2 layer on Mo substrates. Power conversion efficiency (power-to-efficiency) as high as 13.14% with a V_{OC} of 547 mV is achieved for the champion device, which presents a certified efficiency of 12.8% (aperture area: 0.25667 cm^2). Further investigation reveals that Ge bidirectional diffusion simultaneously occurs toward the CZTSSe absorber and $MoSe_2$ layer at the back interface while being selenized. That is, some Ge element from the GeO_2 diffuses into the CZTSSe absorber layer to afford Ge-doped absorbers, which can significantly reduce the defect density and band tailing, and facilitate quasi-Fermi level split by relatively higher hole concentration. Meanwhile, a small amount of Ge element also participates in the formation of $MoSe_2$ at the back interface, thus enhancing the work function of $MoSe_2$ and effectively separating photoinduced carriers. This work highlights the synergistic effect of Ge element toward the bulk absorber and the back interface and also provides an easy-handling way to achieve high-performance CZTSSe solar cells.

1. Introduction

Kesterite $Cu_2ZnSn(S,Se)_4$ (CZTSSe) has been considered as one of the most promising photovoltaic materials due to its high absorption coefficient, adjustable bandgap, stable structure, and earth-abundant, non-toxic, and low-cost constituents.^[1] Very recently, the power conversion efficiency (PCE) of CZTSSe thin-film solar cells has reached 13.0%,^[2] but still far lower than Shockley–Queisser limit efficiency (>30%) and 23.35% efficiency of chalcopyrite $Cu(In,Ga)Se_2$ solar cells.^[3] Comprehensive investigation reveals that the main limitation to the performance of kesterite devices lies in its large open-circuit voltage deficit ($V_{OC,def} = (E_g/q) - V_{OC}$, q is the electron charge). This mainly comes from two aspects: one is suboptimal interfaces including the CdS/CZTSSe interface (front interface) and the CZTSSe/ $MoSe_2$ interface (back interface), the other is a

J. Wang, J. Zhou, X. Xu, L. Lou, K. Yin, B. Duan, H. Wu, J. Shi, Y. Luo, D. Li, Q. Meng
Beijing National Laboratory for Condensed Matter Physics
Renewable Energy Laboratory
Institute of Physics
Chinese Academy of Sciences (CAS)
Beijing 100190, P. R. China
E-mail: dmli@iphy.ac.cn; qbmeng@iphy.ac.cn

J. Wang, J. Zhou, X. Xu, L. Lou, K. Yin, B. Duan, Y. Luo, D. Li, Q. Meng
School of Physical Sciences
University of Chinese Academy of Sciences
Beijing 100049, P. R. China

F. Meng
State Key Laboratory of New Ceramics and Fine Processing
School of Materials Science and Engineering
Tsinghua University
Beijing 100084, China

C. Xiang, H. Xin
State Key Laboratory of Organic Electronics and Information Displays
and Institute of Advanced Materials
Nanjing University of Posts & Telecommunications
Nanjing 210023, China
E-mail: iamhxin@njupt.edu.cn

Y. Luo, D. Li, Q. Meng
Songshan Lake Materials Laboratory
Dongguan, Guangdong 523808, P. R. China

Q. Meng
Center of Materials Science and Optoelectronics Engineering
University of Chinese Academy of Sciences
Beijing 100049, P. R. China

 The ORCID identification number(s) for the author(s) of this article can be found under <https://doi.org/10.1002/adma.202202858>.

DOI: 10.1002/adma.202202858

large amount of defects in the bulk absorber.^[4] Aiming at these issues, various methods have been developed for highly efficient CZTSSe solar cells.

Interface engineering has been widely implemented to reduce the V_{OC} deficit. The front interface often suffers from serious carrier losses caused by the unsatisfied band alignment or high-density interface defects related to secondary phases, crystal distortion, and so on.^[5] For suitable band alignment, people attempted to directly replace CdS buffer layer by other materials (such as ZnCdS, In_2S_3),^[6] insert a passivation layer (i.e., Al_2O_3) or electron-extraction layer (i.e., [6,6]-phenyl- C_{61} -butyric acid methyl ester) (PCBM) between the absorber and the buffer,^[7] or ameliorate the heterojunction property by etching,^[8] post-heat-treatment.^[1b,9] Similarly, for the back interface, undesired energy band arrangement,^[10] numerous voids and secondary phase formation between the Mo and CZTSSe, can easily bring about serious recombination as well as the lower V_{OC} . Generally, it can be restrained to a certain extent by: 1) introducing a high-work-function intermediate layer (i.e., TiN, MoO_x , and ZnO), or 2) increasing the work function of the contact layer with CZTSSe.^[11] However, it is difficult to significantly improve the cell performance of the whole device by interfacial modification alone, no matter whether for the front or back interfaces. At current research stage, more attention has been paid on how to enhance the crystal quality and reduce defects in the bulk CZTSSe.

To the CZTSSe layer, bandgap/potential fluctuation, secondary phases, deep-level defects, band tail states, etc., are mainly responsible for the lower V_{OC} . Except for developing some new solvent systems for good crystalline qualities, incorporating foreign cations for substitution is an effective way to modify the properties of the kesterite itself, even film morphology and interfaces.^[12] For example, Cu–Zn disorder-related defects can be well restrained by using Li^+ or Ag^+ to replace Cu^+ .^[13] Partial substitution of Zn^{2+} with Cd^{2+} was reported to reduce Zn-related deep-level defects and band tail states, thus resulting in longer carrier lifetime.^[14] Typically, Sn-related deep-level defects including Sn_{Zn} antisites and related $[Cu_{Zn} + Sn_{Zn}]$ clusters, are the most deleterious to the V_{OC} of CZTSSe devices. Also, Ge has been proved to be one of the most effective alternative elements to inhibit Sn-related deep-level defects and improve the carrier concentration.^[15] Different Ge incorporation methods have been developed. More Ge-related works were based on Ge-element-involved precursor solutions (i.e., $GeSe_2$, Ge granules, GeO_2 , GeX_2 ($X = Cl, Br, I$)), which exhibited a much better V_{OC} .^[16] Kim et al. demonstrated a Ge-alloyed CZTSe solar cell with 12.3% PCE based on a coevaporation method, in which the $V_{OC,def}$ was improved by reducing the band tailing state and carrier recombination.^[17] Neuschitzer et al. directly evaporated moderate Ge element on magnetron-sputtered Cu/Sn/Cu/Zn metallic stack films and fabricated Ge–CZTSe solar cells with a large increase in V_{OC} .^[18] Recently, double cation incorporation, involving Ge (Ge/Cd, Ge/Na, or Ag/Ge), has also been reported, which enabled better carrier collection efficiency, larger depletion region width, and better optoelectronic properties of the CZTSSe layers.^[19] Although obvious progress in the cell performance has been achieved, Ge incorporation may also bring about other interface or surface defect problems. It is always expected to simultaneously engi-

neer the bulk absorber and the interfaces, which could largely enhance V_{OC} and reduce absorber defects to realize high efficiency devices; however, no related work has been reported to date.

In this work, a wide-bandgap GeO_2 layer has been introduced on the Mo substrate by the spin-coating method for the first time. Ge bidirectional diffusion is found to occur simultaneously toward the CZTSSe absorbers and $MoSe_2$ at back interface in the selenization process. On the one hand, the CZTSSe grain growth is regulated, thus resulting in: i) reduced defect density, ii) suppressed band tailing, and iii) enhanced p-type doping density. On the other, a small amount of Ge is incorporated in $MoSe_2$ to slightly enhance the work function of $MoSe_2$, thereby improving carrier separation at the back interface. This synergistic effect on the bulk and the interface brings about the overall improvement in V_{OC} , J_{SC} , and fill factor (FF), especially the V_{OC} with about 50 mV increased, contributing to the V_{OC}/V_{OC}^{SQ} of 63.1%. Up to 13.14% PCE has been achieved with the V_{OC} of 547 mV for the champion device, which presents a certified efficiency of 12.8% (aperture area: 0.25667 cm^2). Our work provides a new easy-handling synergistic modification method toward the bulk absorber and the back interface by the aid of bidirectional Ge diffusion for highly efficiency CZTSSe solar cells.

2. Results and Discussion

GeO_2 is an air and moisture stable semiconductor material with bandgap of ≈ 5.7 eV, however, it is almost insoluble in most solvents.^[20] In this work, GeO_2 was dissolved in ethanediol/ammonia mixed solvent to afford a GeO_2 precursor solution, which was spin-coated on Mo substrates in the air, followed by annealing at 300 °C to give a uniform layer. Typical Fourier transform infrared (FT-IR) absorption peaks centered at 858 and 572 cm^{-1} , are attributed to the stretching vibration ν_{Ge-O} and bending vibration $\gamma_{Ge-O-Ge}$, respectively, confirming the existence of the GeO_2 (Figure S1a, Supporting Information).^[21] In addition, X-ray photoelectron spectroscopy (XPS) also demonstrates the Ge valence state of +4 in the GeO_2 film with two peaks at 1220 and 1255 eV assigned to the $Ge2p$ core levels and a peak at 532 eV to the $O1s$ core level, respectively (Figure S1b, Supporting Information).^[22] Remarkably, this GeO_2 film is easily dissolved in water and hydrochloric acid, and no X-ray diffraction (XRD) patterns of the GeO_2 are found as well, thus suggesting that the GeO_2 film is in an amorphous state.^[23] The GeO_2 film thickness is determined by its concentration, which is labeled as $n-GeO_2$ (n represents the GeO_2 concentration ($g mL^{-1}$), $n = 0, 0.04, 0.07, 0.10, \text{ and } 0.13$). A Sn^{4+} -dimethyl sulfoxide (DMSO) solution system was directly spin-coated on the top of GeO_2 layer to afford CZTS precursor films, followed by selenization to give CZTSSe absorbers, which were defined as CZTSSe– $n-GeO_2$.^[1c] The selenization process was performed in the rapid heating furnace, where the furnace was first heated to 350 °C in 1 min and held for 5 min, then raised to 545 °C in 5 min and kept for 20 min, finally cooled down naturally to room temperature.

These selenized films with different amounts of GeO_2 were fabricated into solar cells with a configuration of soda–lime

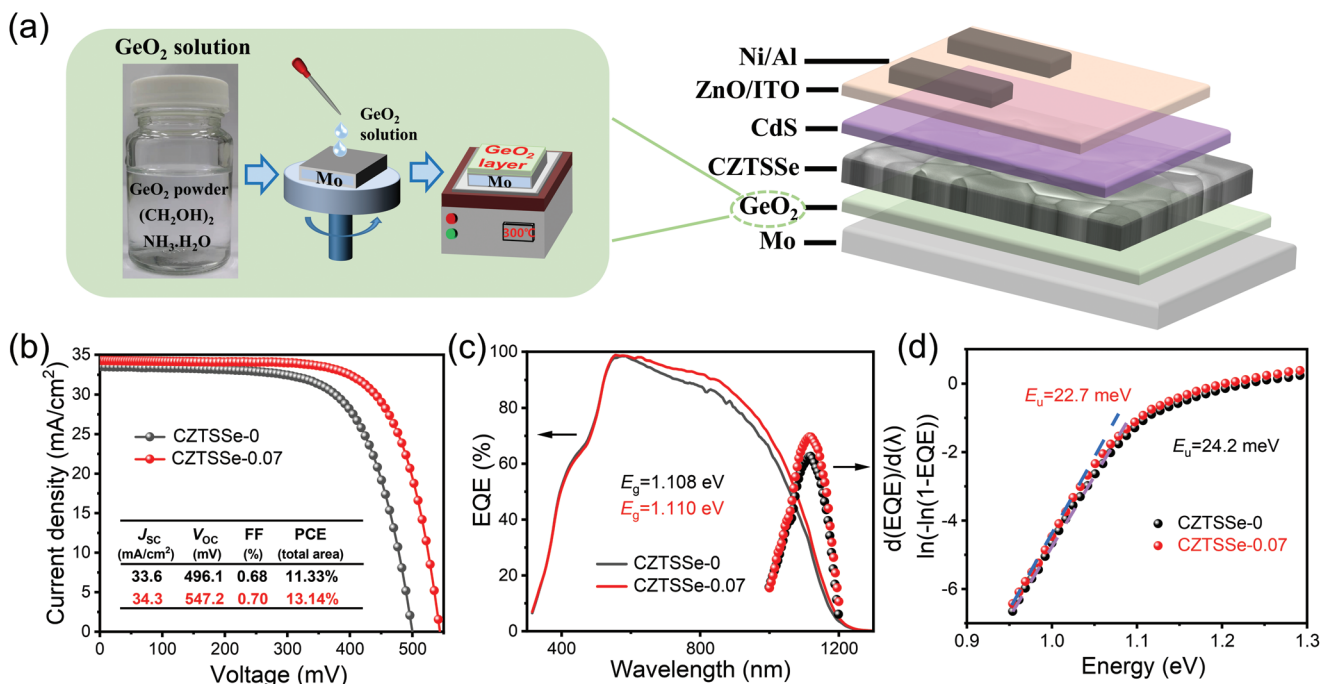


Figure 1. a) Schematic structure of the $\text{Cu}_2\text{ZnSn}(\text{S},\text{Se})_4$ device with GeO_2 layer derived from spin-coating GeO_2 precursor solutions. b) J - V curves and c) EQE spectra and their derivatives of CZTSSe-0- GeO_2 and CZTSSe-0.07- GeO_2 samples. d) Urbach energy of CZTSSe-0- GeO_2 and CZTSSe-0.07- GeO_2 absorbers from EQE spectra.

glass (SLG)/Mo/ GeO_2 /CZTSSe/CdS/ZnO/ITO ($\text{In}_2\text{O}_3:\text{Sn}$)/nickel (Ni)/aluminum (Al) (Figure 1a). In this work, the PCE represents the total area (0.28 cm^2 in our lab) efficiency and all devices were coated by a MgF_2 antireflection layer. According to statistical results of photovoltaic parameters, with the GeO_2 concentration increasing, similar variation tendency of the four parameters (J_{sc} , V_{oc} , FF, and PCE) is found to be first increasing from 0- GeO_2 to the highest (0.07- GeO_2), then decreasing (Figure S2 and Table S1, Supporting Information). Especially for the V_{oc} , the device based on the CZTSSe-0.07- GeO_2 gives the maximum V_{oc} of 547.2 mV with the average V_{oc} of 537.1 mV, much higher than those of the GeO_2 -free one, well consistent with previous reports.^[15b,17] Besides, the highest FF of 0.704 is obtained for the CZTSSe-0.07- GeO_2 -based device, whereas the FF of CZTSSe-0.13- GeO_2 -based device drops to ≈ 0.50 . Therefore, the CZTSSe-0.07- GeO_2 -based device presents the highest average PCE of 12.7%. J - V curves of the best CZTSSe-0- GeO_2 and CZTSSe-0.07- GeO_2 -based devices are presented in Figure 1b. For the best control group, 11.33% PCE is obtained with the J_{sc} of 33.6 mA cm^{-2} , the V_{oc} of 496.1 mV, and the FF of 0.68. The PCE of the CZTSSe-0.07- GeO_2 -based device is enhanced to 13.14% with the J_{sc} , V_{oc} , and FF of 34.3 mA cm^{-2} , 547.2 mV, and 0.70, respectively. Obviously, Ge incorporation is mainly beneficial for the V_{oc} enhancement as well as the J_{sc} slightly improved. Relatively higher V_{oc} and better FF of the CZTSSe-0.07- GeO_2 -based device are also in good agreement with its relatively larger shunt resistance (R_{sh}) and much lower reverse saturation current (J_0) (Table S2, Supporting Information). As we know, for a heterojunction solar cell, the ideality factor reflects the quality of the junction and carrier recombination property.^[24] Here, the ideality factor (A)

of the CZTSSe-0.07- GeO_2 -based device ($A = 1.60$) is smaller than that of CZTSSe-0.07- GeO_2 -based device ($A = 1.81$), suggesting that the trap-assisted recombination can be significantly suppressed as well. On this basis, the certified PCE of 12.8% (certified mask area: 0.25667 cm^2) is obtained with the J_{sc} , V_{oc} , FF of 35.3 mA cm^{-2} , 526 mV, and 0.69, respectively, which is one of the highest results among Ge-involved devices as well as CZTSSe devices (Figure S3, Supporting Information).

According to external quantum efficiency (EQE) spectra in Figure 1c, in comparison with the control group, the EQE of the CZTSSe-0.07- GeO_2 device is almost unaffected in the wavelength region 300–600 nm, but remarkably higher in the longer wavelength range. This discrepancy in the EQE demonstrates that carrier collection ability has been enhanced within the absorber after Ge doping.^[25] Urbach energy (E_U) is estimated from EQE spectra to be 24.2 and 22.7 meV for the control and CZTSSe-0.07- GeO_2 samples, respectively (Figure 1d). Lower E_U is crucial to realize a low $V_{\text{oc,def}}$ and high photovoltaic performance, just in line with our cell performance.^[26] In fact, the bandgaps (E_g) of the CZTSSe-0- GeO_2 (1.108 eV) and CZTSSe-0.07- GeO_2 samples (1.110 eV) are almost unchanged, which is estimated from EQE spectra (Figure 1b). Therefore, unlike other Ge doping/alloying work, the increase in V_{oc} is basically not related to the bandgap, but entirely derived from the reduction in $V_{\text{oc,def}}$. According to the equation $V_{\text{oc}}^{\text{SQ}} = (0.932 \times E_g) - 0.167$, the $V_{\text{oc}}/V_{\text{oc}}^{\text{SQ}}$ is estimated to be 63.1% for the CZTSSe-0.07- GeO_2 device, higher than that of other Ge-involved devices.^[27]

In order to understand the influence of GeO_2 incorporation on the $V_{\text{oc,def}}$, Ge distribution in the bulk CZTSSe or MoSe_2 layer is first investigated. According to XRD patterns,

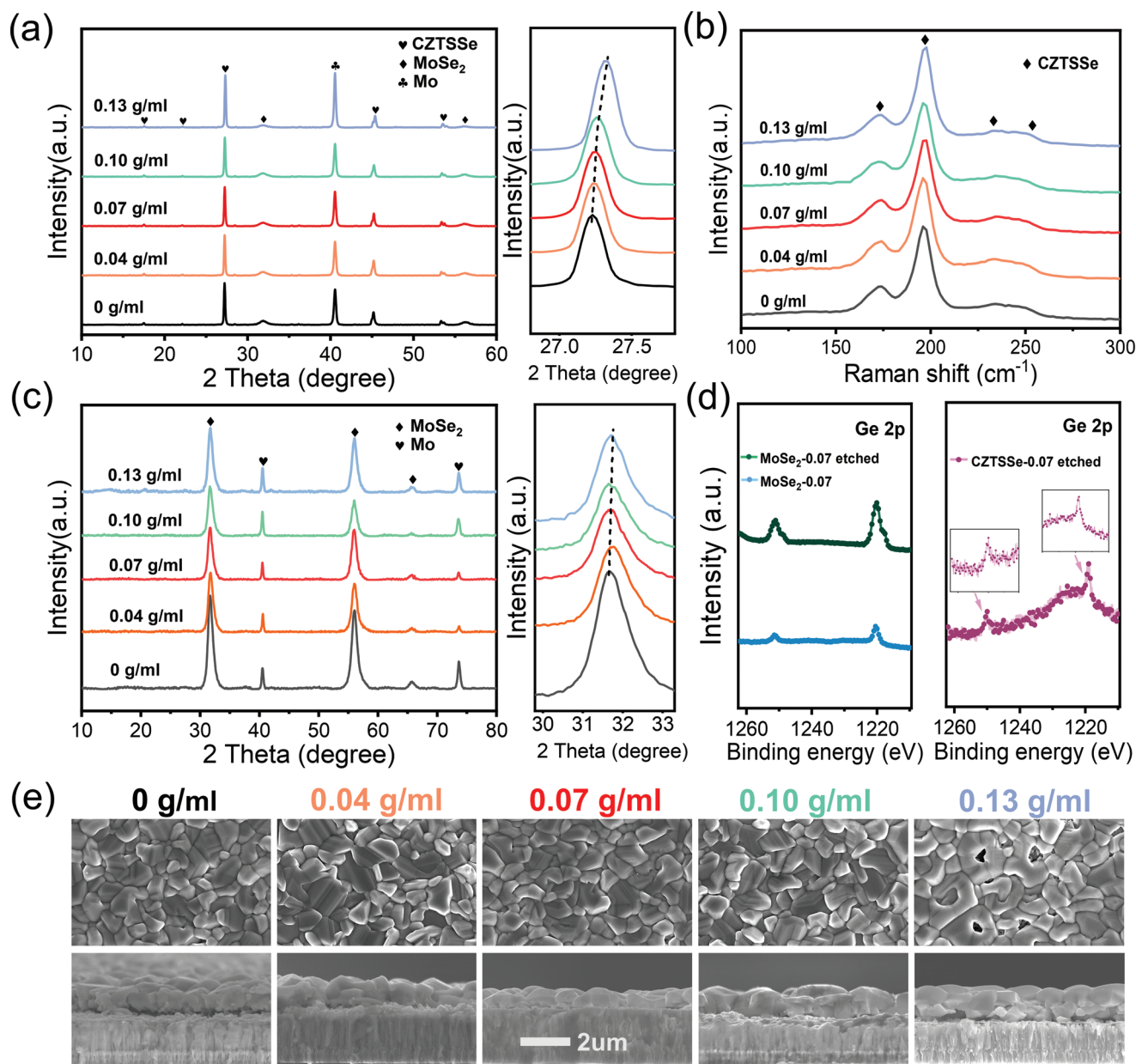


Figure 2. a) XRD patterns of CZTSSe-*n*-GeO₂ films, and expanded (112) peak. b) Raman spectra of CZTSSe-*n* films. c) XRD patterns of MoSe₂-*n*-GeO₂ samples, and their peaks at ≈31.7°. d) XPS core level spectra for MoSe₂-0.07-GeO₂ sample before and after argon etching, and CZTSSe-0.07-GeO₂ film after argon etching with Ge2p elements. e) Top-view SEM images and cross-sectional SEM images of CZTSSe-*n*-GeO₂ films.

no impurity is found in CZTSSe films, no matter if the GeO₂ is involved or not (Figure 2a). With the GeO₂ concentration gradually increasing (0, 0.07 to 0.13), the characteristic (112) diffraction peak assigned to the CZTSSe is slightly shifted to higher angles, indicating that the Ge⁴⁺ with a smaller radius (0.39 Å) enters the absorber layer to substitute Sn⁴⁺ (0.55 Å).^[28] Raman spectra also indicate all the GeO₂-incorporated samples have kesterite structure without secondary phases detectable (Figure 2b).^[29] It is just because a little Ge⁴⁺ is doped into CZTSSe absorber (from the XRD result), the bandgap is slightly increased, thus leading to the *J*_{SC} drop appropriately, especially for CZTSSe-0.13-GeO₂ sample. Besides, to selenized

Mo-*n*-GeO₂ samples (representing GeO₂ layer on Mo substrates), XRD peak of the MoSe₂ at ≈31.7° is found to be slightly shifted to larger angles for the MoSe₂-0.13-GeO₂ in comparison with the MoSe₂-0-GeO₂ sample, suggesting that appropriate Ge⁴⁺ can diffuse down to the MoSe₂ while being selenized (Figure 2c). Scanning electron microscopy with energy-dispersive X-ray spectroscopy (SEM EDS) mapping also indicates the existence of Ge element in both MoSe₂ and CZTSSe absorber (Figure S4, Supporting Information). Also, the Ge distribution has been further investigated by XPS. When the two samples, MoSe₂-0.07-GeO₂ and CZTSSe-0.07-GeO₂ films, were argon etched about 100 nm depth, XPS peaks assigned to Ge2p core

level can still be found with no obvious peak position shifted (Figure 2d). It is thus concluded that the Ge element is indeed bidirectionally diffused down into MoSe₂ and up into CZTSSe absorber. The Ge/(Ge+Sn) ratios are estimated by X-ray fluorescence (XRF) spectra to estimate the Ge amounts in CZTSSe-*n*-GeO₂ (*n* = 0, 0.04, 0.07, 0.10, 0.13) films, which is basically in good accordance with the original feeding ratios (Table S3, Supporting Information).

According to SEM images in Figure 2e, all the CZTSSe-*n*-GeO₂ films have bilayer structure composed of top and bottom large grains, and top grains are obviously larger than the bottom ones.^[30] In addition, CZTSSe grains with a few micrometers in size are densely packed to give smooth CZTSSe-*n*-GeO₂ films except for the CZTSSe-0.13-GeO₂ film with a few voids, which may be leakage paths unfavorable for the cell performance. For the CZTSSe-0-GeO₂ film, some cracks are clearly observed between the CZTSSe layer and MoSe₂ layer, however, this situation can be significantly improved when the GeO₂ is involved, suggesting that the introduction of GeO₂ can improve the back contact, in good accordance with the better FF of the devices. It is noteworthy that, however, for the CZTSSe-0.13-GeO₂ film, a very thin layer appears between the CZTSSe grains and MoSe₂ layer (Figure S5, Supporting Information) accompanied with an abnormal Raman peak at 1300–1700 cm⁻¹, which is assigned to carbon, based on our previous work (Figure S6, Supporting Information).^[31] It is thus supposed that with higher GeO₂ concentration, the interaction between the ethanediol and Ge⁴⁺ may prevent the solvent completely removed under the same selenization condition, thus leaving a thin carbon layer. This

carbon layer may cause larger series resistance, thereby deteriorating device performance.

In order to figure out the impact of Ge doping on carrier recombination and transportation properties of absorber layers, temperature-dependent steady-state photoluminescence (TPL) spectra are obtained in the temperature range from 20 to 140 K (Figure S7, Supporting Information). We can see that, the PL emission peak is redshifted with the temperature increasing. Based on carrier recombination mechanism, the relationship between the PL intensity and the temperature is given as below^[32]

$$I_{\text{PL}}(T) = \frac{I_0}{1 + A_1 \exp\left(-\frac{E_{a1}}{kT}\right) + A_2 \exp\left(-\frac{E_{a2}}{kT}\right)} \quad (1)$$

where I_0 is the PL intensity at the lowest temperature, A_1 and A_2 are fitting parameters, E_{a1} and E_{a2} represent the activation energy of PL quenching due to thermally activated nonradiative transitions, and K is the Boltzmann constant. By fitting the PL intensity with biexponential mode, the E_{a1} and E_{a2} of the CZTSSe-0.07-GeO₂ absorber are estimated to be 29 and 100 meV, respectively, much higher than those of the control group (15 and 69 meV) (Figure 3a). Relatively higher E_a implies that nonradiative recombination can be well suppressed by Ge doping in the absorber, thus leading to less carrier loss.

Furthermore, charge-transport dynamics of CZTSSe-0-GeO₂ and CZTSSe-0.07-GeO₂ solar cells has been investigated by electrical transient technique (Figure 3b,c and Figure S8a,b

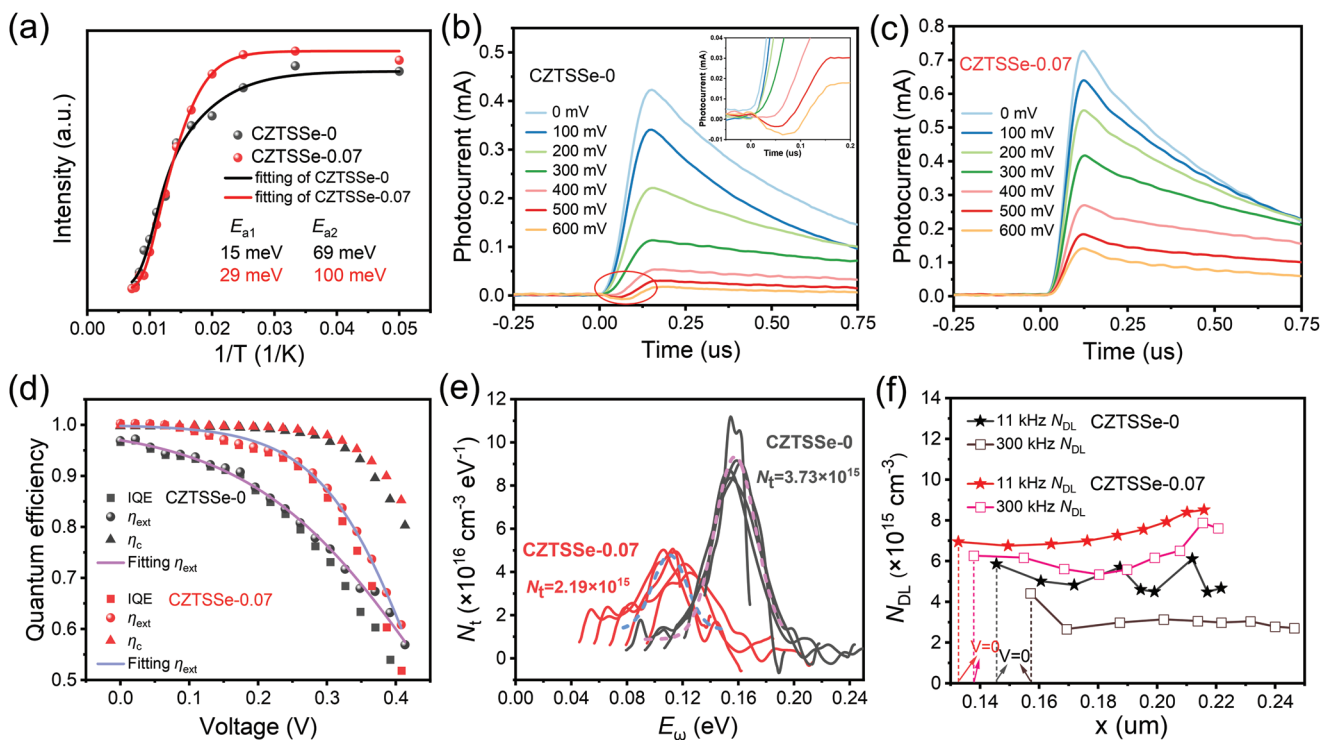


Figure 3. Defect and recombination property characterization of CZTSSe-0-GeO₂ and CZTSSe-0.07-GeO₂-based devices: a) E_a estimated from TPL spectra; b,c) voltage-dependent TPC spectra of CZTSSe-0-GeO₂-based (b) and CZTSSe-0.07-GeO₂-based (c) samples; d) η_c and η_{ext} obtained from TPC and TPV; e) defect densities derived from admittance spectra; f) DLCP results.

(Supporting Information)).^[33] In terms of voltage-dependent transient photocurrent (TPC)/transient photovoltage (TPV) spectra, TPC decay time (τ_{TPC}) and TPV recombination lifetime (τ_{TPV}) are obtained by fitting these decay curves based on a single exponential mode (Figure S8c,d, Supporting Information). When the bias voltage is less than 400 mV, photocurrent variation tendency of the two cells is quite similar with a slight discrepancy. However, to the CZTSSe-0-GeO₂-based device, when the applied bias is equal to or higher than 400 mV, a negative TPC signal appears and this signal intensity gradually increases with the bias voltage increasing. This negative signal is supposed to be mainly related to the electron reverse transmission from the CZTSSe absorber to the bottom layer, which usually occurs in the perovskite solar cell without hole transportation layer.^[34] Instead, this phenomenon is not observed in the CZTSSe-0.07-GeO₂-based device even under higher bias voltages, demonstrating that photoinduced electrons can be efficiently extracted into the front interface due to the improvement of the energy band bending at the back. In addition, the charge collection efficiency (η_c) calculated from the equation: $\eta_c(V) = 1 - (\tau_{\text{TPC}}(V)/\tau_{\text{TPV}}(V))$, is slightly improved at a higher bias voltage, compared to control group, reflecting the performance of the electrode, the absorber (metal–semiconductor contact) and interfacial recombination (Figure 3d).^[33] This suggests that the interfacial contact is improved when the Ge⁴⁺ is involved. Internal quantum efficiency (IQE) is also obtained by using the equation: $\text{IQE}(V) = Q(V)/Q(-1 \text{ V})$, where $Q(V)$ is the integral charge (Figure S8c, Supporting Information). In comparison to CZTSSe-0-GeO₂-based device, CZTSSe-0.07-GeO₂-based device exhibits significantly higher IQE, suggesting faster and more efficient carrier transportation. Additionally, the charge-extraction efficiency (η_{ext}) derived from $\eta_{\text{ext}} = \text{IQE}(V)/\eta_c(V)$ has also been significantly improved (Figure 3d). This further confirms that defects in the bulk Ge-doped CZTSSe can be reduced and the recombination is suppressed as well. The bulk defect state densities (N_t) are derived from fitting the η_{ext} by Equation (2)^[33]

$$\eta_{\text{ext}}(V) = \left[1 + \frac{4\sigma v_{\text{th}} N_t}{D} \left(\frac{L}{\pi} \right)^2 \exp\left(\frac{eV}{Ak_{\text{B}}T} \right) \right]^{-1} \quad (2)$$

where e is the elementary charge, k_{B} is the Boltzmann constant, T is the temperature (300 K), L is the thickness of the CZTSSe absorber (800 nm determined by Profile-system), v_{th} is the thermal velocity calculated from the carrier effective mass ($m^* = 0.1m_0$, m_0 is the electron inertia mass),^[35] D is carrier diffusion coefficient ($1.43 \text{ cm}^2 \text{ s}^{-1}$),^[36] σ is the charge capture cross-section ($1.56 \times 10^{-17} \text{ cm}^2$),^[37] N_t is the defect density, and A is a fitting factor. The N_t is estimated to 8.16×10^{15} and $5.73 \times 10^{14} \text{ cm}^{-3}$ for CZTSSe-0-GeO₂-based and CZTSSe-0.07-GeO₂-based devices.^[38] Obviously, Ge incorporation can bring the bulk defects (possible Sn-related deep-level defects) greatly reduced, an order of magnitude less than the former, which will remarkably reduce nonradiative recombination.

To find defect energy levels in the absorber layer, thermal admittance spectroscopy (TAS) analysis has been conducted to extract the native defect state information by identifying junction capacitance. Here, a series of TAS spectra for

CZTSSe-0-GeO₂- and CZTSSe-0.07-GeO₂-based devices were obtained from 100 to 260 K with a step of 20 K (Figure S9, Supporting Information). The characteristic transition angular frequency (ω_0) is extracted from the derivative of the capacitance–frequency spectrum, and defect activation energy (E_t) is deduced according to Arrhenius plots of $\ln(\omega_0/T^2)$ versus $1/T$. We can see that, when Ge is introduced, E_t of the absorber is reduced from 156.9 to 112.3 meV (Figure S10, Supporting Information). Based on previous work, defects with the activation energy in the range of 0.13–0.2 eV can be assigned to Cu_{Zn} defects.^[37,39] The shallow Cu_{Zn} defect state in the absorber is found in these two devices, but much shallower in the CZTSSe-0.07-GeO₂. That is, to the Ge-involved device, its integrated defect state density is reduced from 3.73×10^{15} (control group) to $2.19 \times 10^{15} \text{ cm}^{-3}$ (Figure 3e). This reduction of defect state densities is supposed to be attributed to stable growth condition owing to cation incorporation.^[17,38] As we know, Cu_{Zn}-related defect cluster [2Cu_{Zn}+Sn_{Zn}] is the culprit of the band tailing. It is thus supposed that Ge incorporation can effectively suppress the formation of the band tailing, consistent with its relatively smaller E_{U} .^[40]

Defect and recombination properties of the two absorbers have also been explored by drive-level capacitance profiling (DLCP) of related CZTSSe devices. As can be seen in Figure 3f, when the Ge is involved, free carrier concentration (N_{DL}) within the absorber increases from 4.42×10^{15} to $6.27 \times 10^{15} \text{ cm}^{-3}$ under high frequency (300 kHz) and zero bias, which is mainly due to the strong interaction between Ge⁴⁺ and Na⁺ during the absorber crystal growth.^[25] Further explanation about the Ge⁴⁺/Na⁺ interaction will be given later. As is widely known, the difference of carrier concentrations between low and high frequencies reflects bulk defect concentration.^[41] Accordingly, bulk defect densities are calculated to be 1.44×10^{15} and $6.74 \times 10^{14} \text{ cm}^{-3}$ for CZTSSe-0-GeO₂- and CZTSSe-0.07-GeO₂-based absorbers, respectively, in good agreement with TPC/TPV results. Furthermore, according to Kelvin probe force microscope (KPFM) images, the CZTSSe-0.07-GeO₂-based absorber exhibits lower surface Fermi level, indicating its higher free carrier concentration, in good accordance with the above DLCP results (Figure S11, Supporting Information). As we know, to p-type materials, relatively lower Fermi level could make the quasi-Fermi level offset more significant while forming a p–n junction, thus resulting in a larger band bending, higher V_{OC} and better cell performance as well.

Based on the above researches, Ge incorporation indeed can reduce defects and the band tailing of the bulk CZTSSe absorber, all of which is related to GeO₂-involved crystallization process. First, the Ge distribution in the absorber has been evaluated as well as the variation tendency during selenization, the CZTSSe-0-GeO₂ and CZTSSe-0.07-GeO₂ films are selected for subsequent scanning transmission electron microscopy (STEM)–EDS mapping investigation. Compositional variations of CZTSSe films and elemental distribution are shown in Figure 4a–d, especially for Ge and O (other elemental distribution is given in Figure S12 in the Supporting Information). Here, two selenization temperatures (350 and 545 °C) are adopted, and CZTSSe-0.07-GeO₂ absorbers selenized over different times labeled as 350 °C-5, 545 °C-10, and 545 °C-20 (i.e., 545 °C-20 representing as selenization at 545 °C

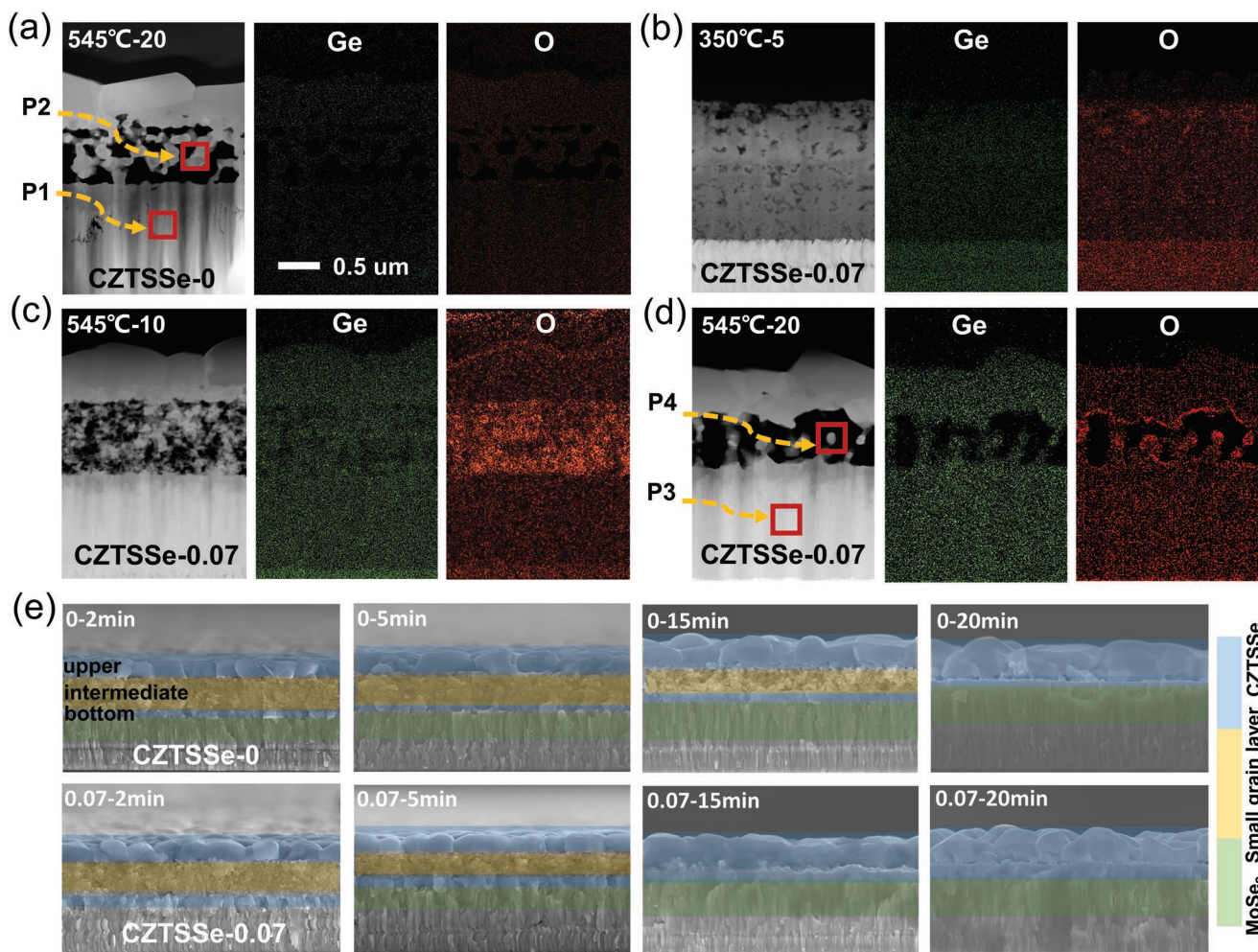


Figure 4. STEM–EDS mapping of Ge and O elements from CZTSSe–0-GeO₂ and CZTSSe–0.07-GeO₂ films: a) CZTSSe–0-GeO₂ film at 545 °C-2000; b) CZTSSe–0.07-GeO₂ film at 350 °C-5; c) CZTSSe–0.07-GeO₂ film at 545 °C-10; d) CZTSSe–0.07-GeO₂ film at 545 °C-20. e) Cross-sectional SEM images of CZTSSe–0-GeO₂ and CZTSSe–0.07-GeO₂ samples selenized at 545 °C for 2, 5, 15, and 20 min.

for 20 min), respectively, represents the evolutionary change of Ge and O distribution in the whole selenization process. For comparison, the CZTSSe–0-GeO₂ absorber at its final selenization state (545 °C-20) is also given. There is no obvious Ge and O signals in the CZTSSe–0-GeO₂ sample (Figure 4a), however, to the CZTSSe–0.07-GeO₂ sample, the contrast between light and shade can be clearly seen under different selenization conditions (Figure 4b–d). For the 350 °C-5 sample, Ge and O are mainly concentrated at the bottom of the precursor film, suggesting that Ge element has not diffused at this moment. When selenized at 545 °C for 10 min (545 °C-10 sample), Ge has already distributed evenly in the whole absorber, whereas the O is mainly concentrated in the unconsumed precursor film. Further extending selenization time to 20 min (545 °C-20), no obvious change in Ge distribution is found and the O element distribution is mainly in the bottom part (between the bottom of large grain layer and the top of MoSe₂ layer) of the CZTSSe absorber, which is confirmed by the secondary-ion mass spectrum (SIMS) in Figure S13 (Supporting Information). Compositional ratios are estimated by single-point measurement in Table S4 (Supporting Information). Four representative posi-

tions (P1, P2, P3, and P4) are selected from CZTSSe–0-GeO₂ and CZTSSe–0.07-GeO₂ samples, respectively. P1/P3 and P2/P4 are located in MoSe₂ layer and at the intersection between the up and bottom large grains, respectively. We can see that, to the CZTSSe–0.07-GeO₂ sample, Ge element can be detectable in MoSe₂ layer although the amount is very small, whereas no Ge element is detectable in the CZTSSe–0-GeO₂ sample. As the GeO₂ is employed as the Ge source, it is necessary to consider the possible role of the O element. Referring previous work, a possible explanation is given as: 1) deep S2 gap states may be eliminated by breaking Se₃–Se₄ wrong bond to give the O_{Se}, thereby improving device performance;^[42] 2) the O may combine with Ge or Sn to form very small amounts of GeO_x and SnO_x nanoinclusions, which act as electron back reflectors to enhance the V_{OC} of the devices.^[43]

To further investigate the influence of GeO₂ on crystallization process, the 545 °C selenization process of CZTSSe–0-GeO₂ and CZTSSe–0.07-GeO₂ samples has been interrupted at different stages to monitor the crystallization progress (Figure 4e). Cross-sectional SEM images tell us that, at the beginning of the selenization, the two samples present a three-layer structure

consisting of the upper large CZTSSe grain layer, the intermediate small grain layer, and the bottom large grain layer. After 2 min selenization, the upper layer thickness is about several hundred nanometers for the two samples, and similar thickness is also observed for the bottom and the middle layers. In the meantime, the MoSe_2 is formed beneath the bottom layer. Further extending the selenization time to 5 min, the upper grains of the two samples get larger, while the MoSe_2 layers become thicker as well, however, the intermediate layer thickness of the CZTSSe-0.07-GeO_2 is about half of that of the CZTSSe-0-GeO_2 . When being selenized over 15 min, the MoSe_2 layer thickness does not change anymore, in the meantime, the intermediate layer of CZTSSe-0.07-GeO_2 sample has already been consumed completely to reach the final state, however, its small grain layer is still left for the CZTSSe-0-GeO_2 sample, while the bottom layer is getting thicker. Obviously, Ge incorporation into the absorber can promote the crystallization rate mainly due to the formation of Ge–Se liquid flux in selenization process.^[12] For the CZTSSe-0-GeO_2 sample, continuous extending selenization time to 20 min can also bring about the final double-layer large grains CZTSSe film without small grains layer anymore, however, for the CZTSSe-0.07-GeO_2 sample, no more change can be found. In addition, under the same selenization time, crystalline grains of the CZTSSe-0.07-GeO_2 sample look smoother and rounder than those of the CZTSSe-0-GeO_2

sample, which is beneficial for the cell performance.^[44] Finally, the evolution of these crystal growth processes is also demonstrated by XRD and Raman spectra. The characteristic (112) kesterite peak of the two samples is gradually left-shifted with the Se gradually replacing the S over the selenization time, and full width at half maxima is reduced as well. Similar variation tendency of Raman spectra is also exhibited (Figure S14, Supporting Information). Of course, the (112) peak position of the CZTSSe-0-GeO_2 and CZTSSe-0.07-GeO_2 films is also slightly different (Figure S14, Supporting Information).

The influence of Ge incorporation on the crystallization and growth processes of the absorber is thus suggested. As shown in Figure 5a, for the CZTSSe-0-GeO_2 sample, the reaction path is basically the same as reported in the literature.^[1c,30a] That is, the amorphous CZTS precursor film directly converts to CZTSSe (so-called small grain layer) by Se substitution reaction at very early selenization stage. With the selenization time extending, the grains become larger both on the top and at the bottom, while the small grain layer is continuously consumed. To CZTSSe-0.07-GeO_2 sample, in its early selenization stage (<2 min), Ge only diffuses upward but does not participate the selenization reaction, thus leading to no obvious difference from the non- GeO_2 sample. When the selenization continues over times, upwardly diffusing Ge starts to merge with the downwardly diffusing Se to form the Ge–Se liquid flux, which

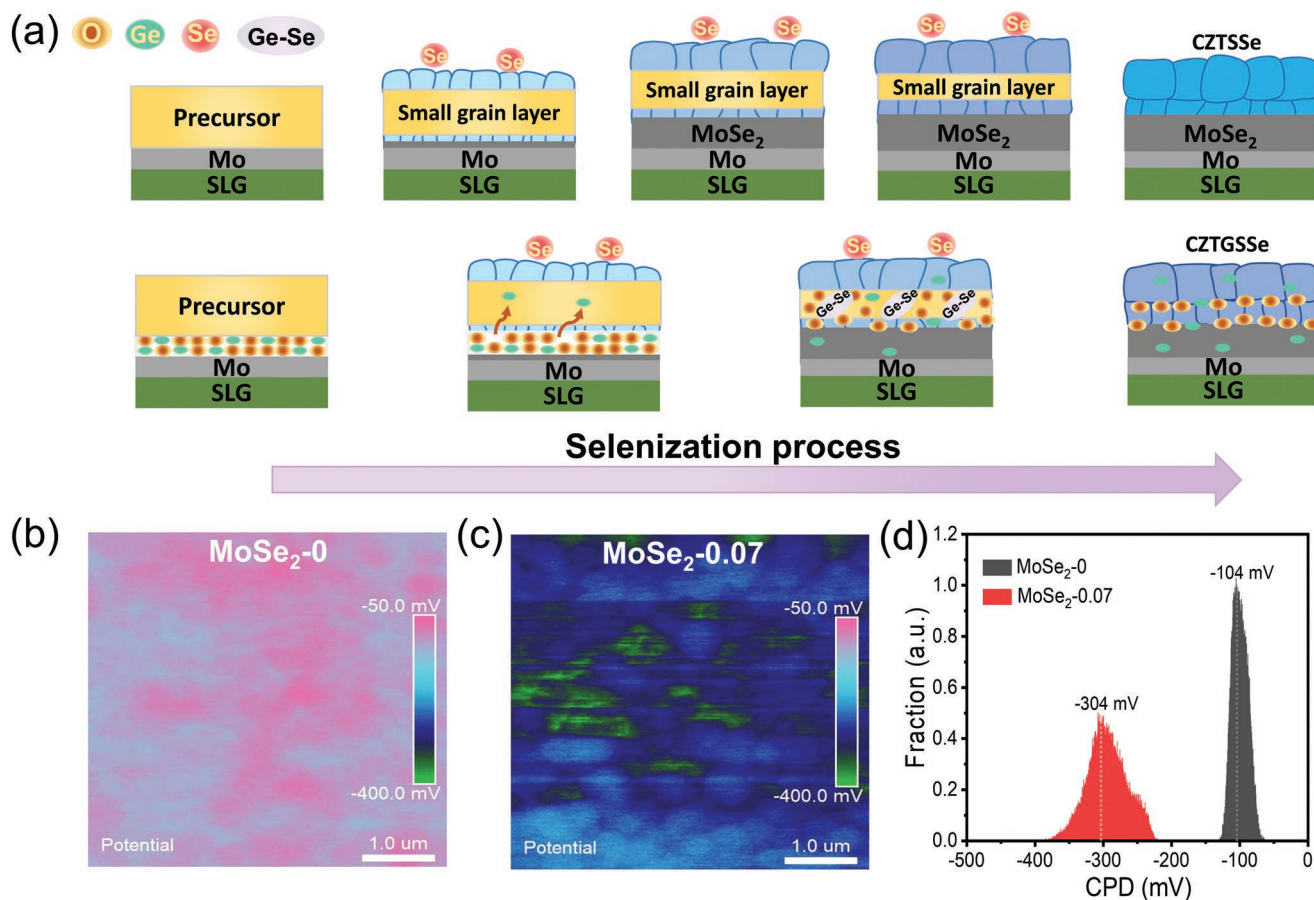


Figure 5. a) Schematic diagrams of CZTSSe crystallization and growth processes without (up) and with GeO_2 (down) Ge incorporation. b, c) Surface potentials of $\text{MoSe}_2-0\text{-GeO}_2$ -based (b) and $\text{MoSe}_2-0.07\text{-GeO}_2$ -based (c) samples and d) average contact potential difference.

will facilitate mass transport in the absorber. Therefore, in the middle and final selenization stages, the crystallization process is significantly accelerated, in the meantime, surface agglomeration and some cracks or holes can also be avoided. Eventually, the Ge distributes evenly in the whole absorber layer and the MoSe₂, whereas the O tends to be enriched at the bottom. Besides, it is supposed that this Ge–Se liquid flux could also dissolve Na-related liquid compounds (i.e., Na₂Se_x), thus facilitating more Na diffusion from the SLG in the absorber and effectively increasing free carrier concentration (N_{DI}) as DLCP result presented.

Ge⁴⁺ also diffuses into the MoSe₂ based on STEM and SIMS results. KPFM images of the two selenized Mo–*n*-GeO₂ samples have been employed to further explore the effect of Ge⁴⁺ on the work function (WF) of the MoSe₂ layer. As shown in Figure 5b,c, the contact potential difference (CPD) distribution of the MoSe₂–0-GeO₂-based sample ranges from –135 to –60 mV, whereas the MoSe₂–0.07-GeO₂-based sample ranges from –400 to –200 mV, their average CPD is –104 and –304 mV, respectively, as shown in Figure 5d. The higher CPD means higher Fermi level and lower WF. Obviously, the introduction of GeO₂ can significantly increase the WF of MoSe₂ by about 200 meV, which mainly comes from Ge⁴⁺ instead of O. However, the WF of MoSe₂ in the CZTSSe-0.07 selenization film is not as high as that of MoSe₂ obtained by direct selenization toward spin-coating GeO₂ on Mo glass, because Ge bidirectional diffusion of the CZTSSe–0.07-GeO₂ film will bring about relatively lower amount of Ge distributed in the MoSe₂ side. This improvement in the WF of MoSe₂ is conducive to a larger energy band upward bending in the CZTSSe absorber, just like an electron barrier, which can help to separate carriers and reduce back recombination, therefore contributing to a higher V_{OC} and J_{SC} .

3. Conclusion

A convenient and effective approach has been developed to simultaneously engineer back interface and bulk defects in the CZTSSe absorber by introducing a GeO₂ layer on Mo substrates for the first time. Up to 13.14% PCE with the V_{OC} of 547 mV has been achieved for the champion CZTSSe device based on an optimal GeO₂ concentration, which can exhibit a certified efficiency of 12.8% (aperture area: 0.25667 cm²). Further investigation reveals that, bidirectional diffusion simultaneously occurs upward to the CZTSSe absorber and downward to MoSe₂ layer while being selenized. That is, in high temperature selenization process, a part of Ge element diffuses to the absorber to combine with Se to form Ge–Se liquid fluxing to promote the nucleation and grain growth, resulting in much flatter CZTSSe films with fewer voids. In addition, bulk defects as well as band tailing are remarkably restrained while the hole concentration is increased, thus achieving less recombination and better Fermi level splitting. In the meantime, another part of Ge diffuses into MoSe₂ layer to increase the work function of MoSe₂, which could be an electron barrier at the back interface to suppress the recombination of photogenerated carriers. As a consequence, the V_{OC}/V_{OC}^{SQ} of the device is 63.1%, which is the lowest $V_{OC,def}$ among all Ge-doped kesterite solar cells

reported so far. This work provides a new idea and an easy-handling method of bidirectional doping to simultaneously modify bulk defects and back interface for high efficiency kesterite solar cells.

4. Experimental Section

Reagents and Materials: GeO₂ powders (99.99%, Aladdin), ethylene glycol (99%, Innochem), ammonia solution (25–28%, Sinopharm Chemical Reagent Co., Ltd.), thiourea (99%, Alfa), DMSO (98%, Alfa), AgCl (99.5%, Innochem), CuCl (99.99%, Alfa), SnCl₄ (99.998%, Macklin), Zn(Ac)₂ (99.99%, Aladdin). All the chemicals were used directly without further purification. SLG was bought from Luoyang Shangzhuo Technology Co., Ltd.

GeO₂ Film Preparation: GeO₂ powders with different masses (0.6, 1.05, 1.5, 1.95 g) were dissolved in a mixed solvent of 10 mL of ethylene glycol and 5 mL of ammonia solution, and stirred vigorously for 1 h to obtain clear GeO₂ solution with concentrations of 0.04, 0.07, 0.10, and 0.13 g mL^{–1}, respectively. The GeO₂ solution was spin-coated on precleaned Mo substrates at 4200 rpm for 40 s, then annealing on a hot plate at 300 °C for 10 s. A thin GeO₂ layer was finally obtained.

CZTSSe Precursor Film Preparation: First, 7.311 g thiourea was added into Vial 1 containing 15 mL DMSO, and stirred until dissolved. Then, 0.345 g AgCl, 2.16 g CuCl were successively added into Vial 1, stirred till completely dissolved. Second, 15 mL DMSO was injected into the Vial 2 containing 3.963 g SnCl₄ under stirring. Then, 3.126 g Zn(Ac)₂ was added into the SnCl₄–DMSO suspension till dissolved completely. Finally, the solution in Vial 2 was poured into Vial 1 to obtain nearly colorless precursor solution. All the above steps were carried out in a N₂-filled glove box.

The filtered precursor solution was spin-coated onto a precleaned Mo substrate or GeO₂-coated Mo substrate by a two-step spin-coating method at 500 rpm for 3 s and another 2000 rpm for 42 s, followed by annealing on a hot plate at 300 °C for 1 min. This coating–annealing process was repeated 7 times to give a precursor film with ≈1.6 μm thickness. Then, precursor films were placed in a graphite box containing Se particles and selenized in a rapid heating tube furnace. The detailed selenization condition was as followed: the temperature was first raised to 350 °C within 1 min and maintained for 5 min, then continuously raised to a higher temperature of 545 °C in 5 min and held for 20 min. The whole selenization process was performed under one atmosphere with N₂ flow of 80 sccm.

CZTSSe Device Fabrication: A 40–50 nm thickness CdS buffer layer was deposited on the top of selenization films by the chemical bath deposition method, followed by radio frequency sputtering to deposit i-ZnO and ITO as a window layer. Ni and Al were deposited by thermal evaporation to complete the whole device. Finally, a MgF₂ layer was thermally evaporated as the antireflection coating, unless specified.

Film Characterization: Fourier transform infrared (FT-IR) absorption spectra were obtained on an FT-IR spectrometer (Bruker, TENSOR 27). XPS measurement was carried out on an ESCALAB 250Xi (Thermo Fisher) instrument, and ≈100 nm depth XPS was also obtained by argon etching for 1000 s. XRD patterns were collected by using an X-ray diffractometer with Cu Kα as the radiation source (Empyrean, PANaltec). Raman spectra were carried out on Raman spectrometer (Lab-RAM HR Evolution, HORIBA) by using 532 nm laser diode as the excitation source. SEM images were measured on a Hitachi S4800 SEM using 10 kV power. The microstructure and elemental distribution of the selenization films were measured by a JEOL-F200CF STEM equipped with an EDS system. Elemental depth compositional profiles of the absorber were determined by secondary-ion mass spectroscopy (TOF-SIMS 5, Germany ION-TOF GmbH). For comparison, an Ar⁺ beam with an impact energy of 20 keV and a beam current of 5 nA was used as the excitation source. Elemental atom ratios were determined by an energy-dispersive XRF spectrometer (EDX-7000, Shimadzu). Temperature-dependent

steady-state PL spectra were obtained on PL spectrometer, FLS 900, Edinburgh Instruments, excited with a picosecond-pulsed diode laser (EPL-445) with the wavelength of 638.2 nm and measured at 730 nm after excitation while cooling down with liquid nitrogen. KPFM images were obtained on an atomic force microscope (Multimode 9, Bruker).

Device Characterization: The current density–voltage (J – V) curves were recorded on Keithley 2400 Source Meter under simulated AM 1.5 sunlight at 100 mW cm⁻² calibrated with a Si reference cell (calibrated by the National Institute of Metrology (NIM)). The 12.8%-efficiency device with aperture area of 0.25667 cm⁻² was independently certified by NIM, China. EQE was measured by Enlitech QE-R test system using calibrated Si and Ge diodes as references. Admittance spectra were recorded on an electrochemical workstation (Versa STAT3, Princeton) at temperature from 100 to 275 K in the dark with the scanning frequency from 1 and 10⁶ Hz. The DLCP was measured on an electrochemical workstation (Versa STAT3, Princeton) by using 11 and 300 kHz AC excitation with amplitude from 10 to 100 mV and with DC bias from 0 to -0.4 V. Modulated transient photocurrent and photovoltage measurements were obtained by our lab-made setup, in which the cell was excited by a tunable nanosecond laser pumped at 532 nm and recorded by a sub-nanosecond resolved digital oscilloscope (Tektronix, DPO 7104) with a sampling resistance of 50 Ω or 1 MΩ.

Statistical Analysis: Statistical analysis was based on the parameters (PCE, V_{OC} , J_{SC} , FF) of 15 devices under the same testing condition (i.e., in the air, room temperature). All data were presented as mean ± standard error of the mean. The sample size (n) for each statistical analysis was the same with the total area (0.28 cm²) for the device efficiency measurement. Data were analyzed and processed by Origin software.

Supporting Information

Supporting Information is available from the Wiley Online Library or from the author.

Acknowledgements

This work was financially supported by the National Natural Science Foundation of China (Grant Nos. U2002216, 51972332, 52172261, 51627803). The authors thank Dr. Yanyan Zhang and Prof. Fuyi Wang from Institute of Chemistry, Chinese Academy of Science for their support of SIMS measurement.

Conflict of Interest

The authors declare no conflict of interest.

Data Availability Statement

Research data are not shared.

Keywords

bidirectional diffusion, CZTSSe solar cells, Ge doping, synergistic effect, V_{OC} deficit

Received: March 29, 2022

Revised: April 19, 2022

Published online:

- [1] a) S. Bag, O. Gunawan, T. Gokmen, Y. Zhu, T. K. Todorov, D. B. Mitzi, *Energy Environ. Sci.* **2012**, *5*, 7060; b) C. Yan, J. Huang, K. Sun, S. Johnston, Y. Zhang, H. Sun, A. Pu, M. He, F. Liu, K. Eder, L. Yang, J. M. Cairney, N. J. Ekins-Daukes, Z. Hameiri, J. A. Stride, S. Chen, M. A. Green, X. Hao, *Nat. Energy* **2018**, *3*, 764; c) Y. Gong, Y. Zhang, Q. Zhu, Y. Zhou, R. Qiu, C. Niu, W. Yan, W. Huang, H. Xin, *Energy Environ. Sci.* **2021**, *14*, 2369; d) J. Li, Y. Huang, J. Huang, G. Liang, Y. Zhang, G. Rey, F. Guo, Z. Su, H. Zhu, L. Cai, K. Sun, Y. Sun, F. Liu, S. Chen, X. Hao, Y. Mai, M. A. Green, *Adv. Mater.* **2020**, *32*, 2005268.
- [2] NREL Best Research-Cell Efficiency Chart, <https://www.nrel.gov/pv/cell-efficiency.html> (accessed: January 2022).
- [3] M. Nakamura, K. Yamaguchi, Y. Kimoto, Y. Yasaki, T. Kato, H. Sugimoto, *IEEE J. Photovoltaics* **2019**, *9*, 1863.
- [4] a) V. Karade, A. Lokhande, P. Babar, M. G. Gang, M. Suryawanshi, P. Patil, J. H. Kim, *Sol. Energy Mater. Sol. Cells* **2019**, *200*, 109911; b) X. Liu, Y. Feng, H. Cui, F. Liu, X. Hao, G. Conibeer, D. B. Mitzi, M. Green, *Prog. Photovoltaics* **2016**, *24*, 879; c) R. Fonoll-Rubio, J. Andrade-Arvizu, J. Blanco-Portals, I. Becerril-Romero, M. Guc, E. Saucedo, F. Peiró, L. Calvo-Barrio, M. Ritzer, C. S. Schnohr, M. Placidi, S. Estradé, V. Izquierdo-Roca, A. Pérez-Rodríguez, *Energy Environ. Sci.* **2021**, *14*, 507.
- [5] a) A. Crovetto, S. Kim, M. Fischer, N. Stenger, A. Walsh, I. Chorkendorff, P. C. K. Vesborg, *Energy Environ. Sci.* **2020**, *13*, 3489; b) N. Physics, K. Kaur, M. Kumar, *J. Mater. Chem. A* **2020**, *8*, 21547.
- [6] a) K. Sun, C. Yan, J. Huang, F. Liu, J. Li, H. Sun, Y. Zhang, X. Cui, A. Wang, Z. Fang, J. Cong, Y. Lai, M. A. Green, X. Hao, *J. Mater. Chem. A* **2019**, *7*, 27289; b) F. Jiang, C. Ozaki, Gunawan, T. Harada, Z. Tang, T. Minemoto, Y. Nose, S. Ikeda, *Chem. Mater.* **2016**, *28*, 3283.
- [7] a) Y. S. Lee, T. Gershon, T. K. Todorov, W. Wang, M. T. Winkler, M. Hopstaken, O. Gunawan, J. Kim, *Adv. Energy Mater.* **2016**, *6*, 1600198; b) J. Park, J. Huang, J. Yun, F. Liu, Z. Ouyang, H. Sun, C. Yan, K. Sun, K. Kim, J. Seidel, S. Chen, M. A. Green, X. Hao, *Adv. Energy Mater.* **2018**, *8*, 1701940; c) L. Lou, Y. Gong, J. Zhou, J. Wang, X. Xu, K. Yin, B. Duan, H. Wu, J. Shi, Y. Luo, D. Li, H. Xin, Q. Meng, *J. Energy Chem.* **2022**, *70*, 154.
- [8] H. Xie, Y. Sanchez, S. Lopez-Marino, M. Espindola-Rodríguez, M. Neuschitzer, D. Sylla, A. Fairbrother, V. Izquierdo-Roca, A. Perez-Rodríguez, E. Saucedo, *ACS Appl. Mater. Interfaces* **2014**, *6*, 12744.
- [9] Z. Su, G. Liang, P. Fan, J. Luo, Z. Zheng, Z. Xie, W. Wang, S. Chen, J. Hu, Y. Wei, C. Yan, J. Huang, X. Hao, F. Liu, *Adv. Mater.* **2020**, *32*, 2000121.
- [10] a) H. J. Gu, J. H. Yang, S. Y. Chen, H. J. Xiang, X. G. Gong, *APL Mater.* **2019**, *7*, 091104; b) M. T. Ferdaous, S. A. Shahahmadi, P. Chelvanathan, M. Akhtaruzzaman, F. H. Alharbi, K. Sopian, S. K. Tiong, N. Amin, *Sol. Energy* **2019**, *178*, 162; c) B. Shin, Y. Zhu, N. A. Bojarczuk, S. Jay Chey, S. Guha, *Appl. Phys. Lett.* **2012**, *101*, 053903.
- [11] a) S. Ranjbar, G. Brammertz, B. Vermang, A. Hadipour, S. Cong, K. Saganuma, T. Schnabel, M. Meuris, A. F. da Cunha, J. Poortmans, *Phys. Status Solidi A* **2017**, *214*, 1600534; b) P. D. Antunez, D. M. Bishop, Y. S. Lee, T. Gokmen, O. Gunawan, T. S. Gershon, T. K. Todorov, S. Singh, R. Haight, *Adv. Energy Mater.* **2017**, *7*, 1602585; c) A. Zhang, Z. Song, Z. Zhou, Y. Deng, W. Zhou, S. Yuan, D. Kou, X. Zhang, Y. Qi, S. Wu, *ACS Appl. Energy Mater.* **2020**, *3*, 10976; d) D. Wang, J. Wu, H. Guo, M. Wu, L. Wu, S. Zhang, J. Ao, H. Wang, Y. Zhang, *Sol. RRL* **2020**, *5*, 2000391; e) J. J. Scragg, T. Kubart, J. T. Wätjen, T. Ericson, M. K. Linnarsson, C. Platzer-Björkman, *Chem. Mater.* **2013**, *25*, 3162; f) S. López-Marino, M. Placidi, A. Pérez-Tomás, J. Llobet, V. Izquierdo-Roca, X. Fontané, A. Fairbrother, M. Espindola-Rodríguez, D. Sylla, A. Pérez-Rodríguez, E. Saucedo, *J. Mater. Chem. A* **2013**, *1*, 8338.

- [12] Y. E. Romanyuk, S. G. Haass, S. Giraldo, M. Placidi, D. Tiwari, D. J. Fermin, X. Hao, H. Xin, T. Schnabel, M. Kauk-Kuusik, P. Pistor, S. Lie, L. H. Wong, *J. Phys.: Energy* **2019**, *1*, 044004.
- [13] a) Y. Gong, R. Qiu, C. Niu, J. Fu, E. Jedlicka, R. Giridharagopal, Q. Zhu, Y. Zhou, W. Yan, S. Yu, J. Jiang, S. Wu, D. S. Ginger, W. Huang, H. Xin, *Adv. Funct. Mater.* **2021**, *31*, 2101927; b) J. Zhou, X. Xu, B. Duan, H. Wu, J. Shi, Y. Luo, D. Li, Q. Meng, *Nano Energy* **2021**, *89*, 106405; c) H. Xin, S. M. Vorpahl, A. D. Collord, I. L. Braly, A. R. Uhl, B. W. Krueger, D. S. Ginger, H. W. Hillhouse, *Phys. Chem. Chem. Phys.* **2015**, *17*, 23859; d) S. G. Haass, C. Andres, R. Figi, C. Schreiner, M. Bürki, Y. E. Romanyuk, A. N. Tiwari, *Adv. Energy Mater.* **2018**, *8*, 1701760; e) Y. Sun, P. Qiu, W. Yu, J. Li, H. Guo, L. Wu, H. Luo, R. Meng, Y. Zhang, S. F. Liu, *Adv. Mater.* **2021**, *33*, 2104330.
- [14] a) C. Yan, K. Sun, J. Huang, S. Johnston, F. Liu, B. P. Veettil, K. Sun, A. Pu, F. Zhou, J. A. Stride, M. A. Green, X. Hao, *ACS Energy Lett.* **2017**, *2*, 930; b) Z. Su, J. M. R. Tan, X. Li, X. Zeng, S. K. Batabyal, L. H. Wong, *Adv. Energy Mater.* **2015**, *5*, 1500682.
- [15] a) S. Giraldo, M. Neuschitzer, T. Thersleff, S. López-Marino, Y. Sánchez, H. Xie, M. Colina, M. Placidi, P. Pistor, V. Izquierdo-Roca, K. Leifer, A. Pérez-Rodríguez, E. Saucedo, *Adv. Energy Mater.* **2015**, *5*, 1501070; b) S. Giraldo, E. Saucedo, M. Neuschitzer, F. Oliva, M. Placidi, X. Alcobé, V. Izquierdo-Roca, S. Kim, H. Tampo, H. Shibata, A. Pérez-Rodríguez, P. Pistor, *Energy Environ. Sci.* **2018**, *11*, 582; c) J. Li, Z.-K. Yuan, S. Chen, X.-G. Gong, S.-H. Wei, *Chem. Mater.* **2019**, *31*, 826.
- [16] a) G. Chen, W. Wang, S. Chen, Z. Whang, Z. Huang, B. Zhang, X. Kong, *J. Alloys Compd.* **2017**, *718*, 236; b) C. J. Hages, S. Levenco, C. K. Miskin, J. H. Alsmeier, D. Abou-Ras, R. G. Wilks, M. Bär, T. Unold, R. Agrawal, *Prog. Photovoltaics* **2015**, *23*, 376; c) G. C. Wessler, T. Zhu, J.-P. Sun, A. Harrell, W. P. Huhn, V. Blum, D. B. Mitzi, *Chem. Mater.* **2018**, *30*, 6566.
- [17] S. Kim, K. M. Kim, H. Tampo, H. Shibata, S. Niki, *Appl. Phys. Express* **2016**, *9*, 102301.
- [18] M. Neuschitzer, M. E. Rodriguez, M. Guc, J. A. Marquez, S. Giraldo, I. Forbes, A. Perez-Rodríguez, E. Saucedo, *J. Mater. Chem. A* **2018**, *6*, 11759.
- [19] a) M. He, J. Huang, J. Li, J. S. Jang, U. P. Suryawanshi, C. Yan, K. Sun, J. Cong, Y. Zhang, H. Kampwerth, M. P. Suryawanshi, J. Kim, M. A. Green, X. Hao, *Adv. Funct. Mater.* **2021**, *31*, 2104528; b) J. Fu, D. Kou, W. Zhou, Z. Zhou, S. Yuan, Y. Qi, S. Wu, *J. Mater. Chem. A* **2020**, *8*, 22292.
- [20] M. Ritter, S. Schönherr, P. Schöppe, W. Wisniewski, S. Giraldo, G. Gurieva, A. Johannes, C. T. Plass, K. Ritter, G. Martínez-Criado, S. Schorr, E. Saucedo, C. Ronning, C. S. Schnohr, *ACS Appl. Energy Mater.* **2019**, *3*, 558.
- [21] a) P. Kitschke, S. Schulze, M. Hietschold, M. Mehring, *Main Group Met. Chem.* **2013**, *36*, 209; b) V. V. Atuchin, T. A. Gavrilova, S. A. Gromilov, V. G. Kostrovsky, L. D. Pokrovsky, I. B. Troitskaia, R. S. Vemuri, G. Carbajal-Franco, C. V. Ramana, *Cryst. Growth Des.* **2009**, *9*, 1829.
- [22] F. Meng, B. Yu, Q. Zhang, Y. Cui, S. Tan, J. Shi, L. Gu, D. Li, Q. Meng, C. Nan, *Adv. Energy Mater.* **2022**, *12*, 2103690.
- [23] O. H. Johnson, *Chem. Rev.* **1952**, *51*, 431.
- [24] a) J. Shi, J. Dong, S. Lv, Y. Xu, L. Zhu, J. Xiao, X. Xu, H. Wu, D. Li, Y. Luo, Q. Meng, *Appl. Phys. Lett.* **2014**, *104*, 063901; b) G. J. Wetzelaer, M. Scheepers, A. M. Sempere, C. Momblona, J. Avila, H. J. Bolink, *Adv. Mater.* **2015**, *27*, 1837.
- [25] S. Giraldo, T. Thersleff, G. Larramona, M. Neuschitzer, P. Pistor, K. Leifer, A. Pérez-Rodríguez, C. Moisan, G. Dennler, E. Saucedo, *Prog. Photovoltaics* **2016**, *24*, 1359.
- [26] J. Chantana, Y. Kawano, T. Nishimura, A. Mavlonov, T. Minemoto, *Sol. Energy Mater. Sol. Cells* **2020**, *210*, 110502.
- [27] A. D. Collord, H. W. Hillhouse, *Chem. Mater.* **2016**, *28*, 2067.
- [28] a) M. Guc, S. Levenco, V. Izquierdo-Roca, X. Fontané, E. Arushanov, A. Pérez-Rodríguez, *J. Appl. Phys.* **2013**, *114*, 193514; b) C. Yang, B. Zhou, S. Miao, C. Yang, B. Cai, W. H. Zhang, X. Xu, *J. Am. Chem. Soc.* **2013**, *135*, 5958.
- [29] a) S. Kim, T. R. Rana, J. Kim, D.-H. Son, K.-J. Yang, J.-K. Kang, D.-H. Kim, *Nano Energy* **2018**, *45*, 75; b) R. Zhang, S. M. Szczepaniak, N. J. Carter, C. A. Handwerker, R. Agrawal, *Chem. Mater.* **2015**, *27*, 2114.
- [30] a) Y. Gong, Y. Zhang, E. Jedlicka, R. Giridharagopal, J. A. Clark, W. Yan, C. Niu, R. Qiu, J. Jiang, S. Yu, S. Wu, H. W. Hillhouse, D. S. Ginger, W. Huang, H. Xin, *Sci. China Mater.* **2021**, *64*, 1304; b) F. Martinho, S. Lopez-Marino, M. Espindola-Rodriguez, A. Hajjafarassar, F. Stulen, S. Grini, M. Dobeli, M. Gansukh, S. Engberg, E. Stamate, L. Vines, J. Schou, O. Hansen, S. Canulescu, *ACS Appl. Mater. Interfaces* **2020**, *12*, 39405.
- [31] X. Xu, L. Guo, J. Zhou, B. Duan, D. Li, J. Shi, H. Wu, Y. Luo, Q. Meng, *Adv. Energy Mater.* **2021**, *11*, 2102298.
- [32] J. Lee, N. C. Giles, D. Rajavel, C. J. Summers, *J. Appl. Phys.* **1995**, *78*, 5669.
- [33] a) J. Shi, D. Li, Y. Luo, H. Wu, Q. Meng, *Rev. Sci. Instrum.* **2016**, *87*, 123107; b) B. Duan, J. Shi, D. Li, Y. Luo, H. Wu, Q. Meng, *Sci. China Mater.* **2020**, *63*, 2371; c) Y. Li, J. Shi, B. Yu, B. Duan, J. Wu, H. Li, D. Li, Y. Luo, H. Wu, Q. Meng, *Joule* **2020**, *4*, 472.
- [34] J. Shi, Y. Li, Y. Li, D. Li, Y. Luo, H. Wu, Q. Meng, *Joule* **2018**, *2*, 879.
- [35] C. Persson, *J. Appl. Phys.* **2010**, *107*, 053710.
- [36] A. Nagaoka, K. Yoshino, H. Taniguchi, T. Taniyama, H. Miyake, *J. Cryst. Growth* **2012**, *354*, 147.
- [37] H.-S. Duan, W. Yang, B. Bob, C.-J. Hsu, B. Lei, Y. Yang, *Adv. Funct. Mater.* **2013**, *23*, 1466.
- [38] S. Kim, K. M. Kim, H. Tampo, H. Shibata, K. Matsubara, S. Niki, *Sol. Energy Mater. Sol. Cells* **2016**, *144*, 488.
- [39] a) P. A. Fernandes, A. F. Sartori, P. M. P. Salomé, J. Malaquias, A. F. da Cunha, M. P. F. Graça, J. C. González, *Appl. Phys. Lett.* **2012**, *100*, 233504; b) S. Chen, A. Walsh, X. G. Gong, S. H. Wei, *Adv. Mater.* **2013**, *25*, 1522.
- [40] K. Nagaya, S. Fujimoto, H. Tampo, S. Kim, M. Nishiwaki, Y. Nishigaki, M. Kato, H. Shibata, H. Fujiwara, *Appl. Phys. Lett.* **2018**, *113*, 093901.
- [41] J. T. Heath, J. D. Cohen, W. N. Shafarman, *J. Appl. Phys.* **2004**, *95*, 1000.
- [42] W.-J. Yin, Y. Wu, S.-H. Wei, R. Noufi, M. M. Al-Jassim, Y. Yan, *Adv. Energy Mater.* **2014**, *4*, 1300712.
- [43] a) S. Bag, O. Gunawan, T. Gokmen, Y. Zhu, D. B. Mitzi, *Chem. Mater.* **2012**, *24*, 4588; b) D. B. Khadka, J. Kim, *J. Phys. Chem. C* **2015**, *119*, 1706.
- [44] C. J. Hages, M. J. Koeper, C. K. Miskin, K. W. Brew, R. Agrawal, *Chem. Mater.* **2016**, *28*, 7703.